The inhomogeneous structure of water at ambient conditions

C. Huang[a], K. T. Wikfeldt[b], T. Tokushima[c], D. Nordlund[a], Y. Harada[c,d], U. Bergmann[a], M. Niebuhr[a], T. M. Weiss[a], Y. Horikawa[c,e], M. Leetmaa[b], M. P. Ljungberg[b], O. Takahashi[f], A. Lenz[g], L. Ojamäe[g], A. P. Lyubartsev[h], S. Shin[c,i], L. G. M. Pettersson[b], and A. Nilsson[a,b,1]

[a]Stanford Synchrotron Radiation Lightsource, P.O.B. 20450, Stanford, CA 94309; [b]FYSIKUM, AlbaNova, and [h]Division of Physical Chemistry, Stockholm University, S-10691 Stockholm, Sweden; [c]RIKEN/SPring-8, Sayo-cho, Sayo, Hyogo 679-5148, Japan; [d]Department of Applied Chemistry, University of Tokyo, Hongo, Bunkyo-ku, Tokyo 113-8656, Japan; [e]Department of Physical Science, Hiroshima University, Higashi-Hiroshima 739-8526, Japan; [f]Department of Chemistry, Hiroshima University, Higashi-Hiroshima 739-8526, Japan; [g]Department of Chemistry, Linköping University, S-581 83 Linköping, Sweden; and [i]Institute for Solid State Physics, University of Tokyo, Kashiwanoha, Kashiwa, Chiba 277-8581, Japan

Edited by H. Eugene Stanley, Boston University, Boston, MA, and approved July 7, 2009 (received for review May 7, 2009)

Small-angle X-ray scattering (SAXS) is used to demonstrate the presence of density fluctuations in ambient water on a physical length-scale of ≈1 nm; this is retained with decreasing temperature while the magnitude is enhanced. In contrast, the magnitude of fluctuations in a normal liquid, such as CCl_4, exhibits no enhancement with decreasing temperature, as is also the case for water from molecular dynamics simulations under ambient conditions. Based on X-ray emission spectroscopy and X-ray Raman scattering data we propose that the density difference contrast in SAXS is due to fluctuations between tetrahedral-like and hydrogen-bond distorted structures related to, respectively, low and high density water. We combine our experimental observations to propose a model of water as a temperature-dependent, fluctuating equilibrium between the two types of local structures driven by incommensurate requirements for minimizing enthalpy (strong near-tetrahedral hydrogen-bonds) and maximizing entropy (non-directional H-bonds and disorder). The present results provide experimental evidence that the extreme differences anticipated in the hydrogen-bonding environment in the deeply supercooled regime surprisingly remain in bulk water even at conditions ranging from ambient up to close to the boiling point.

density fluctuations | liquid–liquid hypothesis | small angle X-ray scattering | water structure | X-ray spectroscopy

Liquid water shows many anomalies in its thermodynamic properties such as compressibility, density variation and heat capacity (1–4). In the low-temperature regime, below the freezing point, these properties deviate strongly from normal and theories, related to a liquid–liquid phase transition between high and low density water, have been proposed to account for these anomalies (5). Although the anomalies are extreme in the supercooled region they are also present at ambient conditions where most of waters' physical, chemical and biological processes of importance occur. In contrast, water at ambient conditions has traditionally been considered as a homogeneous distribution of near-tetrahedral hydrogen-bonded (H-bonded) structures with thermal fluctuations increasing with temperature. This picture has been challenged by recent studies based on X-ray Raman (XRS) and conventional X-ray absorption spectroscopy (XAS) (6), and X-ray emission spectroscopy (XES) (7), suggesting two distinct local structures with tetrahedral as a minority and a highly hydrogen-bond (H-bond) distorted asymmetrical as the majority. In particular the proposed predominant asymmetrical structure has caused intense debate in the last years (see refs. 7 and 8 for detailed discussion).

SAXS and small-angle neutron scattering (SANS) provide the most direct probes of density variations or fluctuations on large length scales in a liquid. Through an enhancement of the structure factor at low momentum transfer, Q, small deviations from the average electron density at different length scales can be reliably identified (9). Previous SAXS studies of water have mostly focused on the supercooled region and given contradictory results where both positive (10–12) and zero enhancement (13, 14) at low Q have been reported. With the development of third-generation synchrotron light sources the ability to perform SAXS has been greatly advanced and measurements can now be performed in a large Q-range with high accuracy and reproducibility (15).

Results

Fig. 1*A* shows the normalized structure factor, $S(Q)$, derived from the SAXS intensity in ambient water (H_2O) as function of Q for temperatures from 7 to 74 °C in the full Q-range of interest, 0.04–0.78 $Å^{-1}$ (see *SI Methods*). All scattering curves show an enhancement approaching $Q = 0$ after experiencing a minimum ≈0.4–0.5 $Å^{-1}$, which to first approximation directly indicates the presence of density heterogeneities. In particular, the enhancement becomes *smaller* with increasing temperature in strong contrast to expectation from simple thermal density fluctuations.

To address whether the enhancement at low Q can be related to and reproduced by thermal fluctuations in common water models, we have performed molecular dynamics (MD) simulations using the extended simple point charge (SPC/E) potential (see *SI Methods*). The SAXS signal at low Q is given by the Fourier transform (FT) of the longer intermolecular correlations in real space from the simulation. To model SAXS data it is thus essential to use large simulation boxes (here 40,000 molecules) and also to average over long simulation runs (here longer than 0.3 ns) to reduce artificial oscillations in Q space. Fig. 1*B* shows the SPC/E oxygen–oxygen partial structure factor, $S(Q)$ (see *SI Methods*). The finite size of the simulation box causes a sharp artificial increase at $Q < 0.13$ $Å^{-1}$ in the FT. The *Inset* shows the results for smaller simulation boxes with 5,000 molecules, where it was possible to average over significantly longer simulation times (2 ns) resulting in smoother curves, but with the FT artificial increase occurring already at $Q = 0.25$ $Å^{-1}$ due to the smaller box size. The most important scattering enhancement observed at small Q in the experiment is completely missing from the SPC/E data even down to $Q = 0.13$ $Å^{-1}$. For comparison, Fig. 1*C* shows $S(Q)$ of CCl_4 measured at temperatures from 6 to 30 °C (see *SI Methods*) and regarded as representing a "normal" liquid. It is clear that SAXS of CCl_4 shows no temperature-dependent

Author contributions: A.N. designed research; C.H., K.T.W., T.T., D.N., Y. Harada, U.B., M.N., T.M.W., Y. Horikawa, M.L., M.P.L., O.T., A.L., L.O., A.P.L., S.S., and L.G.M.P. performed research; C.H., T.T., M.N., and D.N. analyzed data; and C.H., K.T.W., L.G.M.P., and A.N. wrote the paper.

The authors declare no conflict of interest.

This article is a PNAS Direct Submission.

[1]To whom correspondence should be addressed. E-mail: nilsson@slac.stanford.edu.

This article contains supporting information online at www.pnas.org/cgi/content/full/0904743106/DCSupplemental.

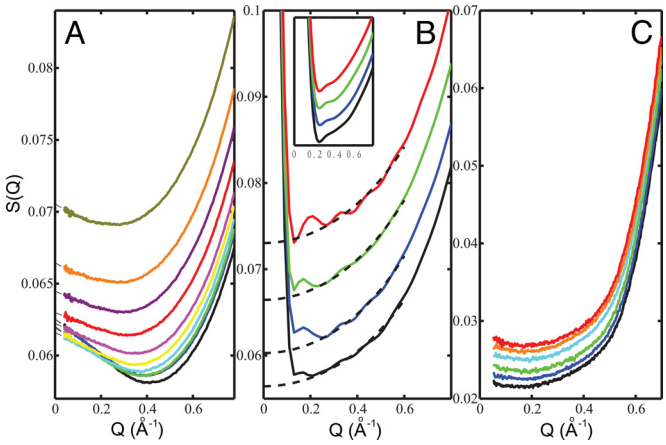

Fig. 1. SAXS results for ambient and CCl_4 liquid compared with SPC/E MD simulations. (*A*) Experimental structure factor, $S(Q)$, derived from small angle water scattering intensity as function of scattering momentum transfer Q. The curves, from bottom to top, correspond to increasing temperatures 7, 11, 16, 20, 25, 29, 38, 47, 56, and 74 °C. The extrapolations of scattering intensity to zero-scattering angle using a second order polynomial fit at low Q are represented by dashed lines. (*B*) The oxygen–oxygen partial structure factor $S(Q)$ for 5, 25, 47, and 67 °C water derived from the SPC/E model using a simulation box containing 40,000 molecules and run for 300–440 ps to reduce artificial oscillations. The mathematical properties of the FT from r to Q space prohibit observation of the behavior below $Q = 0.13$ Å^{-1} when using a box size of 106 Å. (*Inset*) Simulated $S(Q)$ for ambient water from a simulation containing 5,000 water molecules run for 2 ns demonstrating the disappearance of oscillations with extended averaging; the lowest Q accessible is here 0.25 Å^{-1}. The dashed lines indicate smooth curves where the anticipated effects of the box size and limited simulation time are removed. Note the scale of $S(Q)$ in *B* is larger than that in *A* due to steeper monotonically decaying curves for the SPC/E water compared with the experimental data. (*C*) Experimental $S(Q)$ of CCl_4 liquid as function of Q. The curves, from bottom to top, correspond to increasing temperatures 6, 11, 16, 21, 25, and 30 °C.

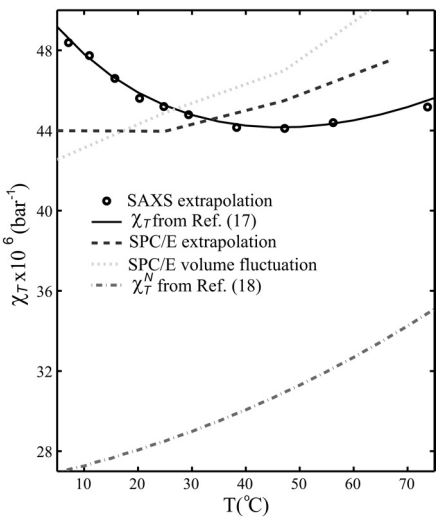

Fig. 2. Isothermal compressibility of water, χ_T, derived by extrapolating measured $S(Q)$ at $Q = 0.04$–0.2 Å^{-1} to $Q = 0$ Å^{-1} (dots) compared with a previous experimental dataset determined from the sound velocity in water (17) (full line). Estimated χ_T from the SPC/E simulations (NVT ensemble) based on an extrapolation of $S(Q)$ to $Q = 0$ Å^{-1} for the 40,000 molecule model (dashed line) and direct estimation of χ_T for SPC/E simulations in the NPT ensemble equilibrated 7 ns and sampled over 5 ns (dotted line). The normal contribution of the isothermal compressibility, χ_T^N, extracted from a previous experimental dataset determined by the sound velocity in water–ethanol mixtures (18).

variation at low Q, which is observed, in contrast, in the ambient water as shown in Fig. 1*A*. Furthermore, the Q dependence from the SPC/E simulation is closer to the experimental data for CCl_4 than for water demonstrating that the observed enhancement of the SAXS signal at low Q for water is not due to normal thermal fluctuations as obtained from standard MD simulations.

Extrapolating the structure factor in Fig. 1*A* to $Q = 0$ (dashed curves) by means of a second order polynomial fit to the experimental $S(Q)$ in the range $Q = 0.04$–0.2 Å^{-1} we can relate to the isothermal compressibility, χ_T, of water at each temperature (16) via the thermodynamical relation

$$S(0) = k_B T n \chi_T, \qquad [1]$$

where k_B is the Boltzmann constant, T is the absolute temperature, and n is the molecular number density. We verify our SAXS data and extrapolation by comparing in Fig. 2 χ_T derived from the present SAXS data with χ_T from an earlier study (17) measuring the velocity of sound in water; an absolute agreement is observed, confirming the quality of our data and that the density heterogeneities are related to fluctuations in the H-bonded network. If we also extrapolate the 40,000 molecules SPC/E simulations to $Q = 0$, we determine χ_T as a function of temperature (Fig. 2) and find instead a linear relationship indicative of normal liquid behavior (3, 18, 19), i.e., without the minimum at 46 °C and increase at lower temperatures. Consistent results are obtained using an alternative estimation of χ_T from volume fluctuations in the NPT ensemble in SPC/E simulations run for 12 ns with 7 ns equilibration time, which exhibit a similar trend with temperature as a previous estimation using the NVT ensemble (20). This directly demonstrates that density fluctuations existing in a standard water model such as SPC/E do not reproduce the observed density heterogeneities that the experimental SAXS and isothermal compressibility data clearly indicate. In Fig. 2 we also compare the SPC/E results with the contribution of normal liquid behavior of water to the isothermal compressibility, as estimated from ref. 18, and find a similar temperature dependence albeit shifted in absolute value. It is thus clear that the observed fluctuations in ambient water should be different from random thermal motion and instead similar to what has been discussed in the supercooled regime (10–12).

To gain further insight we analyze the SAXS data within the framework of Ornstein-Zernicke (OZ) theory (21) assuming the density fluctuations to result from the presence of either a spinodal (22) or critical point (5). To apply the OZ theory we follow Conde et al. (18) and Kanno and Angell (19) and decompose the total scattering structure factor $S(Q)$ into a part $S^N(Q)$ associated with "normal liquid" behavior and an anomalous part $S^A(Q)$ associated with critical phenomena. We assume that the "normal liquid" part of the scattering factor at $Q = 0$, $S^N(0)$, is given by Conde's normal contribution to the isothermal compressibility, χ_T^N (see Fig. 2) via Eq. **1**. We further assume that the high Q region (>0.7 Å^{-1}) lacks an anomalous contribution because it is dominated by near-neighbor scattering. Based on this we represent $S^N(Q)$ by a second order polynomial fitted to $S^N(0)$ and all data points between $Q = 0.74$–0.78 Å^{-1}, as shown in Fig. 3*A*. The anomalous component $S^A(Q)$ is then obtained as the difference between the experimental data and the thus estimated $S^N(Q)$.

Within the OZ framework, the anomalous part is described by

$$S^A(Q) = \frac{c}{\xi^{-2} + Q^2}, \qquad [2]$$

where ξ is the correlation length defined in the OZ theory and c depends on temperature but not on Q (21). To derive ξ we fitted $S^A(Q)$ between $Q = 0.04$–0.19 Å^{-1} with results plotted in Fig. 3*B*

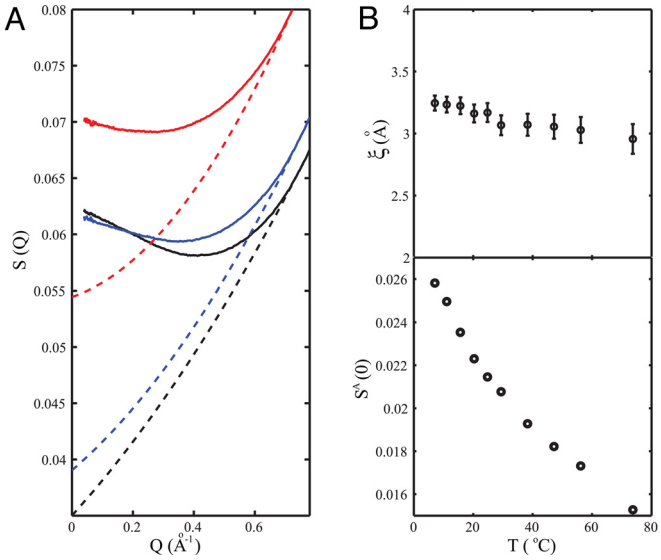

Fig. 3. Ornstein-Zernicke (OZ) analysis of SAXS results of ambient water. (*A*) The estimation of ''normal liquid'' contributions, $S^N(Q)$(dashed lines), to the total scattering factor, $S(Q)$(solid lines), at 7 (black), 25 (blue) and 74 °C (red) by using the method described in the text, i.e., $S^N(Q)$ is derived by fitting $S(Q)$ between Q = 0.74–0.78 Å^{-1} and $S^N(0)$ using a second order polynomial function. (*B*) (*Upper*) OZ correlation length ξ defined in Eq. **2** as function of temperature. (*Lower*) The derived $S^A(0)$ as function of temperature.

Upper as function of temperature; the OZ correlation length is ≈3.1 Å, slowly decreasing with increasing temperature. The zero-angle anomalous structure factor, $S^A(0) = c\xi^2$, is, however, found to decrease more dramatically with temperature as shown in Fig. 3*B Lower*.

X-ray spectroscopies give further insight into the character of the density heterogeneities indicated by SAXS. In both XES (7) and XRS (6) it has recently been shown that there are temperature-dependent spectral changes that can be connected to the H-bonded environment. XRS corresponds to transitions from a core level to unoccupied states, while XES measures the decay from an occupied valence state to an emptied (excited) core level with the emission of an X-ray photon. Although the valence electrons are delocalized in a condensed phase, the involvement of the core level makes both XRS and XES very local probes of the electronic structure (23). Furthermore, the attosecond time scale of the XRS excitation process and the O 1*s* life time of ≈4 fs in XES (24) are much shorter than the 1–2 ps typical for H-bond dynamics (25).

The focus for our discussion will be how the experimental XES and XRS spectra of water vary with temperature and how the energy position of the spectral features relates to similar features in water vapor and ice. Fig. 4*A* shows the temperature dependence in the lone pair $1b_1$ region of the XES spectra for D_2O (see *SI Methods*); using the heavier isotope minimizes core-hole induced dynamical effects on the spectral line shape (7, 26). All spectra show a split of the lone pair into two peaks, in ref. 7 denoted $1b_1'$ and $1b_1''$, where the former is close in energy position to the $1b_1$ in crystalline ice and the latter to $1b_1$ in water vapor. The two peaks can thereby be related to tetrahedral ($1b_1'$) and H-bond distorted ($1b_1''$) local structures with further support for this assignment given below. Fig. 4*B Upper* part shows the temperature-dependent XRS spectra with higher energy resolution (0.5 eV) (see *SI Methods*) compared with earlier studies (6). The spectral features in XRS and XAS of liquid water and ice have been denoted pre-edge (535 eV), main-edge (537–538 eV) and postedge (540–541 eV) (6). Crystalline ice exhibits a strong postedge whereas gas phase water has nearly all of the intensity in the pre- and main-edge regions (27).

We use energy-selective excitation to make a connection between the two X-ray spectroscopies. The XES spectra shown in Fig. 4*A* were all taken with excitation at 550 eV, well beyond the region with structure-dependent spectral features in the absorption spectrum. Tuning instead the energy to the specific resonant features (pre-, main- and postedge) in the absorption spectrum makes a connection between the two X-ray spectroscopies by selecting the corresponding structural species for XES (7). This is shown in Fig. 4*C* where resonant XES spectra are compared with nonresonant (550 eV) XES. Normalizing the intensities to the $1b_1''$ (distorted) peak, we find that pre-edge

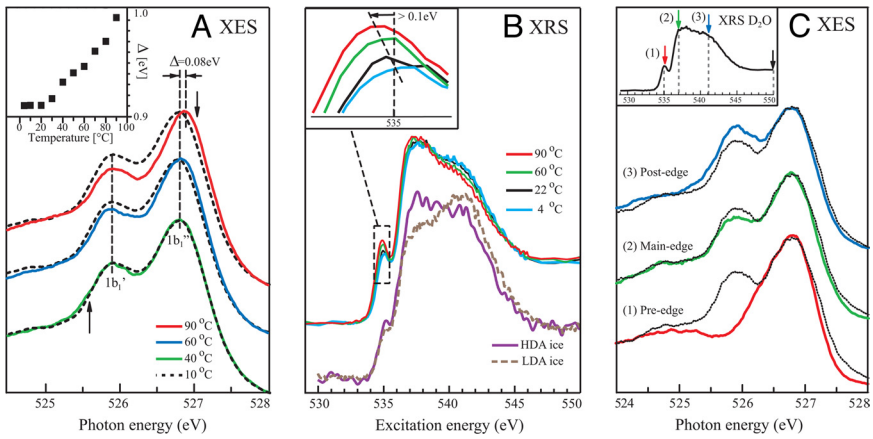

Fig. 4. XES/XRS spectra of ambient water and amorphous ice. (*A*) The lone pair $1b_1$ region of the O 1*s* soft X-ray emission spectra of liquid D_2O at 10, 40, 60 and 90 °C using a nonresonant excitation energy of 550 eV. The positions of the corresponding $1b_1$ state of crystalline ice (525.6 eV) and gas phase water (527 eV) are indicated with arrows (7). The two lone pair peaks in liquid water are denoted, respectively, $1b_1'$, close to the corresponding position in crystalline ice, and $1b_1''$, close to gas phase water. The $1b_1'$ peak position is independent of temperature whereas the $1b_1''$ shifts toward higher energy with increasing temperature. The spectra were normalized to give the same $1b_1''$ peak height. (*Inset*) Energy difference between the $1b_1''$ and $1b_1'$ peaks as function of temperature. (*B*) (*Upper*) X-ray Raman scattering spectra of liquid H_2O at 4, 22, 60 and 90 °C normalized to have the same area. (*Inset*) Magnification of the pre-edge (535 eV) spectral feature indicating a shift toward lower energy with increasing temperature. (*Lower*) XRS spectra of LDA and HDA ice from ref. 33. (*C*) X-ray emission spectra at various excitation energies (full lines) compared with nonresonant excitation (dashed lines) at 550 eV of D_2O water at 25 °C. (*Inset*) XRS spectrum of D_2O with arrows marking the corresponding excitation energies. Note that the pre-edge excited spectrum has been shifted by 0.45 eV to compensate for the spectator shift of a localized excited intermediate state (7).

excitation essentially eliminates the $1b_1'$ (tetrahedral) peak (red), excitation on the main edge gives a slight enhancement of the $1b_1''$ (distorted) (green), whereas excitation on the postedge instead enhances the $1b_1'$ (tetrahedral) peak compared with the $1b_1''$ (blue). Because the absorption postedge feature in ice is much stronger than in the liquid (6), the resonant XES (blue) is consistent with that the $1b_1'$ peak is related to tetrahedral-like species. The pre-edge peak in XRS has, however, been assigned to distorted H-bonding configurations (6, 27–31). This assignment is consistent with the observed absence of the $1b_1'$ (tetrahedral) and the strong enhancement of the $1b_1''$ (distorted) peak when resonantly exciting on the pre-edge feature (red).

The assignment is furthermore fully consistent with the experimentally observed temperature dependence of both XRS and XES: In XRS, the postedge decreases and the pre-edge increases with increasing temperature (see Fig. 4*B*), similar to the postedge-associated $1b_1'$ converting to the preedge-associated $1b_1''$ in XES. Hence, both XES and XRS indicate in a consistent manner that water consists of two distinct, interconverting structural species in a ratio that depends on temperature. This is also within the range of possible structures that X-ray and neutron diffraction data allow, as shown in a recent analysis using reverse Monte Carlo modeling (32).

There is another important temperature effect in the XES and XRS spectra indicating changes beyond the interconversion of the two structural species. Both the $1b_1''$ (distorted) peak in XES (Fig. 4*A*) and the related pre-edge feature in XRS (Fig. 4*B*) shift toward their respective gas phase position with increasing temperature whereas neither the $1b_1'$ (tetrahedral) in XES nor the broad postedge feature in XRS shows measurable changes in energy position. This implies that the distorted structural species successively become more distorted with increasing temperature through thermal excitation whereas the tetrahedral-like species do not significantly change their H-bonding. Consequently, a variation in the relative stability of the two structures with temperature is expected.

We fitted the XES spectra at each temperature into two spectral components to obtain the intensity ratio $I_{1b1''}/I_{1b1'}$ between distorted and tetrahedral structures; at 25 °C we obtain 2.5 ± 0.5 where the error bar is mainly due to systematic shifts based on different assumptions on the line shapes (see ref. 7 for detailed description). If the energy (ΔE) and entropy (ΔS) differences do not depend on temperature, an Arrhenius behavior is expected, i.e., a plot of the ratio, $ln(I_{1b1''}/I_{1b1'})$, between the contributions from the two structural components to the XES spectra versus the inverse temperature ($1/T$), should give a straight line with the average energy difference (ΔE) obtained from the slope:

$$\ln(I_{1b1''}/I_{1b1'}) = -\frac{\Delta E}{RT} + \frac{\Delta S}{R}. \qquad [3]$$

Fig. 5 plots $ln(I_{1b1''}/I_{1b1'})$ versus the inverse temperature ($1/T$), where the derivative of the fitted curve is shown in the *Inset*. We note that the data do deviate from a straight line, indicating that ΔE and ΔS vary with temperature between the two local structures. Because the tetrahedral structure in both XES and XRS shows little spectral change with temperature we can assume that the ΔE and ΔS variation are mainly attributable to changes of the distorted structure. The conversion of tetrahedral-like to distorted with temperature shows that the tetrahedral-like component is of lower energy. The shifting of $1b_1''$ position in XES and the pre-edge in XRS with temperature indicate an increase in entropy of the distorted component as it becomes thermally excited. All of these observations are consistent with that the tetrahedral structure is of lower energy - lower entropy and the distorted structure of higher energy–higher entropy.

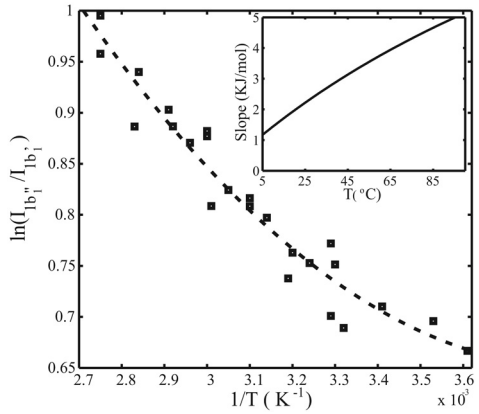

Fig. 5. Plot of the logarithm of the intensity ratio between the fitted XES spectra of $1b_1''$ and $1b_1'$ versus the inverse temperature, 1/T. The dashed line is a guide to the eye, where the slope is not constant. The slope is shown versus temperature in *Inset*.

A recent XRS study of ambient water and high density (HDA) and low density amorphous ice (LDA) identified similarities in the liquid water spectrum with that of HDA ice (33) (see Fig. 4*B Lower*). Based on these spectra it can be hypothesized that the H-bond distorted structure, which dominates liquid water at ambient conditions, corresponds to a thermally excited and volume expanded HDA phase whereas the tetrahedral-like structures are related to LDA. The LDA spectrum can be linked to the tetrahedral structure in water through the strong postedge seen in XRS on LDA ice and through the low energy XES $1b_1'$ component in water with energy position close to that of crystalline ice (see Fig. 4*A*).

Discussion and Conclusions

We analyze further the density fluctuations in the SAXS data in terms of the picture indicated by XES and XRS, namely that, on the time scale of X-ray scattering, the liquid can be viewed as tetrahedral patches surrounded by thermally excited H-bond distorted structures. Although we lack information on the time scale of the fluctuations, the attosecond interaction time of the X-ray scattering process, compared with picoseconds for H-bond dynamics, allows considering the SAXS data as an instantaneous snapshot of the structure. Because we do not detect any major contribution of intermediate structures in neither the XES nor the XRS data we make the simple approximation that the SAXS intensities are mainly connected with a density difference contrast between the two structural species seen as static on the ultrashort time scale of the scattering process. Consequently, we infer a physical picture of the derived OZ correlation length ξ (Fig. 3*B Upper*) in terms of the radius of gyration, R_G, defined in the Guinier analysis developed for static macroparticle scattering (9). The relationship $R_G = \sqrt{3}\xi$ (34) gives R_G decreasing from 5.6 at 7 °C to 5.1 Å at 74 °C. To get a sense of the physical dimensions of the tetrahedral patches we assume a spherical shape giving a diameter, D, of 14.5–13.2 Å by using the relationship $D = 2\sqrt{5/3}R_G$ (35). In an earlier light-scattering measurement providing Raman density of states (36), a cross-over frequency between the phonon and fracton regimes has been observed, suggesting the existence of low-density water patches of dimension ≈10–14 Å at 22 °C, similar to the present result.

We can conclude the following experimental observations: On the time scale of the scattering and spectroscopic processes two local structural species coexist with tetrahedral-like patches of dimension of order 1 nm in dynamic equilibrium with H-bond distorted and thermally excited structures. Both the characteristic dimension based on SAXS and the local structure of the

tetrahedral-like component based on XES/XRS are relatively insensitive to temperature whereas that of the H-bond distorted component continuously changes as it becomes thermally excited and expands, leading to loss of contrast in SAXS (Fig. 3*B Lower*). Combining the SAXS and spectroscopy information we infer that the tetrahedral-like patches form as low energy-low entropy structures of lower density than the average of the liquid. The higher density, thermally excited H-bond distorted structure, however, is a high entropy structure where the higher density compensates the loss of enthalpy through a larger number of, but less specific, H-bond interactions.

The picture of ambient water presented here contains many similarities to models describing the anomalies of supercooled water based on a liquid–liquid phase transition between high and low density water (2, 4, 5). The current experimental results indicate that the liquid–liquid transition affects a larger neighborhood in the P-T phase diagram than anticipated, surprisingly extending far into the ambient regime creating an inhomogeneous fluctuating structure. In particular, the domination of the distorted structure in the liquid can be understood because high-density water is on the ambient side of the phase separation, or Widom line (37, 38) (defined as an extension of the coexistence line between low- and high-density liquid in the "one-phase region" for the second critical point scenario (5)), whereas the tetrahedral structure is on the low-temperature side. This is in line with the similar line shape seen in XRS between HDA and water at ambient conditions as shown in Fig. 4*B* (33) and the observation using infrared spectroscopy of a low density liquid phase in supercooled confined water at temperatures below the Widom line (39). It can furthermore be linked to the previous, much discussed Wernet et al. study (6), because even at room temperature the dominating high-density high-entropy structure can be expected to be highly thermally excited. This would result in much larger H-bond distortions for the distorted than for the tetrahedral component of the liquid, as suggested for the asymmetric species proposed in that study.

The detailed structure of the two types of species reported in the present work and the time scale on which these fluctuations exist, creating temperature-dependent density and structural heterogeneities even in ambient liquid water, are not yet precisely determined, however.

Materials and Methods

The SAXS experiments were performed at beamline 4-2 at the Stanford Synchrotron Radiation Lightsource (SSRL) using a beam energy of 11 keV. A quantum mechanically calculated molecular scattering factor of an isolated water molecule (40) was used to separate $S(Q)$ from the total scattering intensity. The XRS experiments were performed at beamline 6–2 at SSRL, equipped with a Si (311) double crystal monochromator and the Raman scattering was analyzed using 14 Si (440) analyzer crystals selecting 6.46 keV photons with a resolution of ≈0.3 eV and momentum transfers of $Q = 2.6 \pm 1$ Å^{-1}. The O 1s XES measurements (7) were performed with a total energy resolution of 0.35 eV at BL17SU at SPring-8, Japan. Detailed description of the experimental and computational methods is described in the *SI Methods*.

ACKNOWLEDGMENTS. We thank H. C. Andersen and H. Wennerström for critically reading an earlier version of the manuscript. This work was supported by U.S. National Science Foundation Grants CHE-0809324 and CHE-0431425, the Swedish Foundation for Strategic Research, the Swedish Research Council, the Swedish National Supercomputer Center, and the Japanese Ministry of Education, Science, Sports and Culture through a Grant-in-Aid for Scientific Research. Portions of this research were carried out at the Stanford Synchrotron Radiation Lightsource (SSRL), a national user facility operated by Stanford University on behalf of the U.S. Department of Energy, Office of Basic Energy Sciences.

1. Angell CA (2008) Insights into phases of liquid water from study of its unusual glass-forming properties. *Science* 319:582–587.
2. Brovchenko I, Oleinikova A (2008) Multiple phases of liquid water. *Chem Phys Chem* 9:2660–2675.
3. Debenedetti PG (2003) Supercooled and glassy water. *J Phys Condens Matter* 15:R1669–R1726.
4. Mishima O, Stanley HE (1998)The relationship between liquid, supercooled and glassy water. *Nature* 396:329–335.
5. Poole PH, Sciortino F, Essmann U, Stanley HE (1992) Phase-behavior of metastable water. *Nature* 360:324–328.
6. Wernet P, et al. (2004) The structure of the first coordination shell in liquid water. *Science* 304:995–999.
7. Tokushima T, et al. (2008) High resolution X-ray emission spectroscopy of liquid water: The observation of two structural motifs. *Chem Phys Lett* 460:387–400.
8. Leetmaa M, et al. (2008) Diffraction and IR-Raman do not prove tetrahedral water/ *J Chem Phys* 129:084502.
9. Koch MHJ, Vachette P, Svergun DI (2003) Small-angle scattering: A view on the properties, structures and structural changes of biological macromolecules in solutions. *Quart Rev BioPhys* 36:147–227.
10. Bosio L, Teixeira J, Stanley HE (1981) Enhanced density fluctuations in supercooled H_2O, D_2O, and ethanol-water solutions: Evidence from small angle X-ray scattering *Phys Rev Lett* 46:597–600.
11. Xie Y, Ludwig KF, Morales G, Hare DE, Sorensen CM (1993) Noncritical behaviour of density fluctuations in supercooled water. *Phys Rev Lett* 71:2050–2053.
12. Bosio L, Teixeira J, Bellissent-Funel MC (1989) Enhanced density fluctuations in water analyzed by neutron scattering. *Phys Rev A* 39:6612–6613.
13. Dings J, Michielsen JCF, Van der Elsken J (1992) Equilibrium and nonequilibrium contributions to X-ray scattering from supercooled water. *Phys Rev A* 45:5731–5733.
14. Michielsen JCF, Bot A, van der Elsken J (1988) Small-angle X-ray scattering from supercooled water. *Phys Rev A* 38:6439–6441.
15. Smolsky IL, et al. (2007) Biological small angle X-ray scattering facility at Stanford Synchrotron Radiation Laboratory. *J Appl Cryst* 40:s453–s458.
16. Hendrick RW, Mardon PG, Shaffer LB (1974) X-Ray Zero-Angle Scattering Cross-Section of Water. *J Chem Phys* 61:319–322.
17. Kell GS (1970) Isothermal compressibility of liquid water at 1 atm. *J Chem Eng Data* 15:119–122.
18. Conde O, Teixeira J, Papon P (1982) Analysis of sound velocity in supercooled H_2O, D_2O, and water–ethanol mixtures *J Chem Phys* 76:3747–3753.
19. Kanno H, Angell CA (1979) Water: Anomalous compressibilities to 1.9 kbar and correlation with supercooling limits. *J Chem Phys* 70:4008–4016.
20. Motakabbir KA, Berkowitz M (1990) Isothermal compressibility of SPC/E water. *J Phys Chem* 94:8539–8562.
21. Hansen JP, McDonald IR (2006) *Theory of Simple Liquids* (Elsevier, London).
22. Speedy RJ (1982) Stability-limit conjecture. An interpretation of the properties of water. *J Phys Chem* 86:982–991.
23. Nilsson A, Pettersson LGM (2004) Chemical bonding on surfaces probed by X-ray emission spectroscopy and density functional theory. *Surf Sci Reps* 55:49–167.
24. Neeb M, Rubensson JE, Biermann M, Eberhardt W (1994) Coherent excitation of vibrational wave-functions observed in-core hole decay spectra of O_2, N_2 and CO. *J El Spec Rel Phenom* 67:261–274.
25. Nibbering ETJ, Elsaesser T (2004) Ultrafast vibrational dynamics of hydrogen bonds in the condensed phase. *Chem Rev* 104:1887–1914.
26. Fuchs O, et al. (2008) Isotope and temperature effects in liquid water probed by X-ray absorption and resonant X-ray emission spectroscopy. *Phys Rev Lett* 100:027801.
27. Myneni S, et al. (2002) Spectroscopic probing of local hydrogen bonding structures in liquid water. *J Phys Condens Matter* 14:L213–L219.
28. Iannuzzi M (2008) X-ray absorption spectra of hexagonal ice and liquid water by all-electron Gaussian and augmented plane wave calculations. *J Chem Phys* 128:204506.
29. Odelius M, Cavalleri M, Nilsson A, Pettersson LGM (2006) X-ray absorption spectrum of liquid water from molecular dynamics simulations: Asymmetric model. *Phys Rev B* 73:024205.
30. Prendergast D, Galli G (2006) X-ray absorption spectra of water from first principles calculations. *Phys Rev Lett* 96:215502.
31. Smith JD, et al. (2004) Energetics of hydrogen bond network rearrangements in liquid water. *Science* 306:851–853.
32. Wikfeldt KT, Leetmaa M, Ljungberg MP, Nilsson A, Pettersson LGM (2009) On the Range of Water Structure Models Compatible with X-ray and Neutron Diffraction Data. *J Phys Chem B* 113:6246–6255.
33. Tse JS, et al. (2008) X-ray Raman spectroscopic study of water in the condensed phases. *Phys Rev Lett* 100:095502.
34. Teixeira J (1992) Introduction to small angle neutron scattering applied to colloidal science in *Structure and Dynamics of Supramolecular Aggregates and Strongly Interacting Colloids*, eds Chen SH, Huang JS, Tartaglia P (Kluwer, Drordrecht).
35. Guinier A, Fournet G (1955) *Small Angle Scattering of X-rays* (John Wiley & Sons, New York).
36. Majolino D, et al. (1993) Spectral evidence of connected structures in liquid water: Effective Raman density of vibrational states. *Phys Rev E* 47:2669.
37. Kumar P, et al. (2007) Relation between the Widom line and the breakdown of the Stokes-Einstein relation in supercooled water *Proc Nat Acad Sci USA* 104:9575–9579.
38. Xu L, et al. (2005) Relation between the Widom line and the dynamic crossover in systems with a liquid–liquid phase transition *Proc Natl Acad Sci USA* 102:16558–16562.
39. Mallamace F, et al. (2007) Evidence of the existence of the low-density liquid phase in supercooled, confinded water *Proc Natl Acad Sci USA* 104:424–428.
40. Wang J, Tripathi AN, Smith JVH (1994) Chemical binding and electron correlation effects in X-ray and high energy electron scattering. *J Chem Phys* 101:4842–4854.

Supporting Information

Huang et al. 10.1073/pnas.0904743106

SI Methods

Small-Angle X-Ray Scattering. The SAXS experiments were performed at beamline 4–2 at the Stanford Synchrotron Radiation Lightsource (SSRL) using a beam energy of 11 keV and an optical fiber coupled CCD detector (MarCCD165) (1). For water measurements, a quartz capillary sample holder with a diameter of 1.5 mm was integrated into the vacuum setup eliminating the need for additional windows between the beam defining slit and the exit window of the flight path. The sample holder, detector and the path in between were placed in a vacuum of 1×10^{-3} torr to reduce the background scattering. For CCl_4 measurements, 400-μm thick CCl_4 is sandwiched by two 10-μm thick mica windows. Both water and CCl_4 sample devices were connected to a constant temperature bath, within which water was circulated to maintain and control the sample temperature. Data were collected at three different sample-detector lengths, covering the range of the scattering vector, defined as $Q = 4\pi\sin\theta/\lambda$, between 0.04 to 0.78 Å^{-1}, where λ is the wavelength and θ is one-half of the scattering angle. To reduce the possibility of radiation damage, the data were continuously collected for 10 frames with 1 min each and all scattering images were averaged afterward. The scattering curves have been corrected for the primary beam intensity, absorption and detector readout noise. The scattering of the empty capillary at each temperature was measured separately and subtracted. The water scattering was observed to be ≈80% of the total scattering at $Q = 0.05$ Å^{-1}. Thus, the capillary scattering subtraction is very reliable.

X-Ray Raman Scattering. The XRS experiments were performed at beamline 6–2 at SSRL, equipped with a Si (311) double crystal monochromator. Raman scattering was analyzed with a high-energy-resolution multicrystal analyzer in a Rowland geometry (R = 1 m) using 14 Si (440) analyzer crystals (100 mm in diameter) at a fixed Bragg angle of 88°. This setup selects 6.46 keV photons with a resolution of ≈0.3 eV and momentum transfers of $Q = 2.6 \pm 1$ Å^{-1}. The monochromator energy was scanned from 6,990 to 7,060 eV with a flux of $\approx 3 \times 10^{12}$ photons/sec focused down to a 0.1×1 mm^2 spot size. The overall energy resolution amounted to 0.5 eV full width at half maximum (FWHM). Approximately 40 scans were averaged for each temperature with a total count of ≈15,000 to 20,000 per averaged spectrum. Energy calibration was checked periodically by recording the elastic peak before and after a given temperature point. To correct for energy drift between the elastic peak calibration points, for each temperature, the scans were energy-calibrated to the noncalibrated sum of each series, resummed and calibrated again. We estimate that the relative energy calibration is accurate to within ± 0.025 eV. The water was flowed through an aluminum cell with a 5×5 mm^2 Si_3N_4 window of 1-μm thickness. The X-ray path from the beampipe to the detector (including the whole sample cell) was kept in 1 atm He to avoid background scattering from air.

X-Ray Emission Spectroscopy. The O 1s XES measurements (2) were performed with a total energy resolution of 0.35 eV at BL17SU at SPring-8, Japan. A 150-nm-thick Au-coated Si_3N_4 window was used to separate the liquid flow from the high vacuum and to transmit the incoming and outgoing soft X-rays; coating the window with Gold and using a sample flow rate of 20 mm/sec were important to eliminate radiation damage. For precise alignment of the XES spectra of the three forms of water, i.e., ice, liquid and gas phase water, we used the same XES spectrometer while replacing the liquid cell by other sample mounts for ice and gas phase water.

Molecular Dynamics Simulations. The SPC/E (3) simulations were performed using the parallelized MD code MDynaMix5.0 (4). We used simulation boxes with 40,000 molecules in the NVT ensemble, resulting in box lengths of ≈106 Å and using the experimental densities at each temperature. An NPT simulation at 25 °C was also performed and seen to give the same small-angle scattering as in the NVT ensemble. Simulation boxes with 5,000 molecules were first equilibrated and then replicated periodically into $2 \times 2 \times 2$ supercells. These large boxes were further equilibrated for at least 50 ps to eliminate artificial periodicity. Because the oxygen atom positions in the simulations correspond very well to the center of mass of the molecular charge densities, the oxygen–oxygen pair-correlation function, $g(r)$, should contain all of the information on long-range heterogeneities if present. The $g(r)$ was calculated up to $r_{max} = \sqrt{2}\cdot L$Å (where L is half the box length) by using interatomic distances out to the edges of the simulation box, and then Fourier transformed to obtain the partial structure factor according to

$$S(Q) = 1 + 4\pi\rho \int_0^{r_{max}} \varpi(r) r^2 [g(r) - 1] \frac{\sin Qr}{Qr} dr, \qquad [4]$$

where ρ is the average number density of water at the given temperature and $\varpi(r)$ is a modification function that replaces truncation ripples in the FT with a single unphysical bell-shaped bump at small Q the width of which is inversely proportional to the maximum distance used in $g(r)$ (5). Finally, the derived $S(Q)$ were averaged over between 300 ps (67 °C) and 440 ps (5 °C) in the production stage of the simulations.

As an independent check of the validity of our simulated small-angle scattering intensity, we compared the isothermal compressibility obtained according to Eq. **1** after extrapolating the simulated S(Q) down to $Q = 0$ with results obtained by the fluctuation formula

$$\chi_T = \frac{\langle V^2 \rangle - \langle V \rangle^2}{k_B T \langle V \rangle}. \qquad [5]$$

Very long simulations in the NPT ensemble are required for convergence in χ_T. Here, simulations with 512 SPC/E water molecules were performed at 5, 25, 47 and 67 °C for 12 ns, and the last 5 ns were used to calculate χ_T.

1. Smolsky IL, et al. (2007) Biological small angle X-ray scattering facility at Stanford Synchrotron Radiation Laboratory. *J Appl Cryst* 40:453–458.
2. Tokushima T, et al. (2008) High resolution X-ray emission spectroscopy of liquid water: The observation of two structural motifs. *Chem Phys Lett* 460:387–400.
3. Berendsen HJC, Grigera JR, Straatsma TP (1987) The missing term in effective pair potentials. *J Phys Chem* 91:6269–6271.
4. Lyubartsev AP, Laaksonen A (2000) M. DynaMix—a scalable portable parallel MD simulation package for arbitrary molecular mixtures. *Comput Phys Comm* 128:569–589.
5. Waser J, Schomaker V (1953) The Fourier inversion of diffraction data. *Rev Mod Phys* 25:671–690.